# Efficient Plane-Wave Approach to Generalized Kohn-Sham Density-Functional Theory of Solids with Mixed Deterministic/Stochastic Exchange

Tucker Allen, Barry Y. Li, Tim Duong, and Daniel Neuhauser*

*Department of Chemistry and Biochemistry, University of California, Los Angeles, CA, 90095, USA*

(Dated: March 11, 2025)

An efficient mixed deterministic/sparse-stochastic plane-wave approach is developed for band-structure calculations of large supercell periodic generalized-Kohn-Sham density functional theory, for any hybrid-exchange density functional. The method works for very large elementary cells and supercells, and we benchmark it on covalently bonded solids and molecular crystals with non-bonded interactions, for supercells of up to 33,000 atoms. Memory and CPU requirements scale with supercell size quasi-linearly.

Generalized Kohn-Sham density functional theory (GKS-DFT), i.e., DFT with hybrid exchange-correlation (XC) functionals that include exact exchange, is now a cornerstone of electronic structure methods as such functionals reduce the self-interaction error of local- and semi-local DFT for both solids and molecules.[1–3] These functionals, particularly screened hybrids that separate short- and long-range exchange, [4] capture the fundamental physics in both classes of systems.[5–7] Tuned hybrids control the balance between short- and long-range exchange through a range-separation parameter, $\gamma$, which is commonly obtained through either empirical fitting or first-principles calculation, e.g., by enforcing Koopmans' theorem. [8] For solids, short-range screened hybrids such as HSE06 yield bandgaps and lattice constants in good agreement with experiment for both semiconductors and insulators.[9, 10] Another commonly used functional, the PBE0 global hybrid, uses a fixed fraction of exact exchange chosen based on perturbation theory arguments.[11, 12] For molecules, long-range corrected (LC) hybrids enable proper description of charge-transfer and excitonic effects.[4, 13] Additionally, dielectric-dependent hybrids have been successfully applied.[14–16]

Exact exchange scales usually quadratically with the number of $k$-points $N_k$. Many approaches have been developed to reduce the cost of evaluating exact exchange in both finite and extended systems.[17–23] However, efficient treatment of global and long-range hybrids that include a $G = 0$ singular part of the exchange kernel remains a challenge as a larger $k$-point mesh is required to converge observables to the thermodynamic limit.

In this Letter, we develop an efficient reciprocal-space plane-wave (PW) implementation of GKS-DFT. A cheap and accurate construction of the $k$-dependent exchange matrix is achieved for both small and very large unit cells. We introduce a general fitting procedure that uses the (semi)local-DFT wavefunctions sampled at the Brillouin zone center ($k = 0$, the $\Gamma$-point) as a basis for the true $k$-dependent molecular orbitals (MOs) required for evaluating exact exchange. Then, to enable GKS-DFT calculations of large unit- and super-cells we implement a mixed deterministic/sparse-stochastic approach, splitting the exchange kernel into low- and high-momentum components, using our near-gap hybrid-DFT (ngH-DFT) approach for molecules.[24]

The starting point is a GKS-Hamiltonian

$$H = K + V_{eN} + v_H + X + v_{xc}, \quad (1)$$

with the usual kinetic, nuclear, and Hartree terms; $X$ is the Fock operator under a general explicit exchange kernel $v$,

$$X(r, r') = -\rho(r, r')v(r - r'), \quad (2)$$

and $v_{xc}(r)$ is a (semi)local-DFT XC potential for a kernel $|r - r'|^{-1} - v(r - r')$. The explicit exchange kernel is usually made from short- and long-range parts, [1, 4]

$$v(r - r') = \frac{\alpha + \beta \cdot \text{erf}(\gamma|r - r'|)}{|r - r'|}. \quad (3)$$

Various functionals are used here including global Becke-type and range-separated hybrids that employ Fock exchange at short-range, long-range, or a mixture of both, see Table I.

The periodic near-gap formalism starts analogously to the non-periodic approach described in Refs.[24, 25]. Here, lower-case functions and coordinates refer to the supercells, and upper-case ones are used within a single unit (elementary) cell. The initial step is a cheap LDA (or a general DFT for local or semi-local functional) calculation for periodic systems on a supercell with $N_k$ unit cells, which yields $k$-space zero-order periodic MOs, labeled $|\Phi_{pk}\rangle$.

The global Bloch states, $\phi_{pk}(r) = \frac{1}{\sqrt{N_k}}e^{ikr}\Phi_{pk}(r)$, are orthogonal on the supercell:

$$\langle\phi_{nk}|\phi_{n'k'}\rangle \equiv \int_{\text{supercell}} \phi^*_{nk}(r)\phi_{n'k'}(r)dr = \delta_{kk'}\delta_{nn'}, \quad (4)$$

while for the same $k$, the upper-case functions are orthogonal within a single unit cell,

$$\langle\Phi_{nk}|\Phi_{n'k}\rangle \equiv \int_{\text{elem.cell}} \Phi^*_{nk}(R)\Phi_{n'k}(R)dR = \delta_{nn'}. \quad (5)$$

A "band" of active orbitals near the Fermi level is then taken, and labeled as "near-gap" states. Specifically, for each $k$-point we divide the states into several types: $N_{\text{core}}$ (lower valence) states (which are of course above the inner-core states that are part of the norm-conserving pseudopotential (NCPP)); $N_v = N_{\text{occ}} - N_{\text{core}}$ upper valence; and $N_c$ low-lying conduction states.

The $M \equiv N_v + N_c$ near-gap orbitals are labeled as the MO-active space. Further, we introduce a subspace $A \subseteq M$, with $A \equiv A_v + A_c$, and $A_v (\leq N_v)$ and $A_c (\leq N_c)$ valence and conduction MOs, for which exchange is calculated explicitly. $A$ is labeled as the exchange-active space. The effect of the core states on the exchange is approximated as a perturbative scissor correction, discussed later.

The GKS eigenstates on the supercell are then expanded in terms of zero-order MOs from the same $k$-point:

$$|\psi_{ik}\rangle = \sum_j C_{ji}^k |\phi_{jk}\rangle, \qquad (6)$$

where most integer indices extend over the $M$ active orbitals, with a similar $|\Psi_{ik}\rangle = \sum_j C_{ji}^k |\Phi_{jk}\rangle$ relation for a single unit cell.

For each $k$, $C^k$ is an eigenvector matrix of the $k$-dependent Hamiltonian matrix:

$$H_{jl}^k \equiv \langle \phi_{jk} | H | \phi_{lk} \rangle \equiv h_{jl}^k + X_{jl}^k, \qquad (7)$$

where as usual,

$$h_{jl}^k = \langle \Phi_{jk} | \frac{(k + \hat{G})^2}{2} + V_{eN} + v_H + v_{xc} | \Phi_{lk} \rangle. \qquad (8)$$

Further

$$X(r, r') = -\sum_{m\bar{k}} f_{m\bar{k}} \psi_{m\bar{k}}(r) v(r - r') \psi_{m\bar{k}}^*(r'), \qquad (9)$$

where the orbital occupations are introduced.

For the purpose of the exchange matrix elements only, we expand the $k$-dependent elementary functions in terms of the $\Gamma$-point functions (see also Ref.[26])

$$|\Phi_{jk}\rangle \simeq \sum_{j'} B_{j'j}^k |\Phi_{j'}\rangle, \qquad (10)$$

where $|\Phi_{j'}\rangle \equiv |\Phi_{j',k=0}\rangle$. Thus, when used in the exchange part,

$$|\Psi_{jk}\rangle \simeq \sum_{j'} D_{j'j}^k |\Phi_{j'}\rangle, \qquad (11)$$

where $D^k = C^k B^k$. Thus, $X^k = (B^k)^\dagger Y^k B^k$, where $Y^k$ is the momentum-space representation of the exchange matrix with the zero-order basis, which reads:

$$Y_{jl}^k = -\frac{1}{N_k^2} \sum_{m\bar{k}m'm''} f_{mk} D_{mm'}^{\bar{k}} D_{mm''}^{\bar{k},*} \iint dr dr' \\ \Phi_j(r) \Phi_{m'}(r) e^{-i(k-\bar{k})(r-r')} v(r - r') \Phi_{m''}(r') \Phi_l(r'), \qquad (12)$$

where the $\Gamma$-point wavefunctions are real-valued. The momentum-space representation is readily shown to be:

$$Y_{jl}^k = -\sum_{i\bar{k}G} z_{jGi\bar{k}}^* z_{lGi\bar{k}} v(G - k + \bar{k}), \qquad (13)$$

with rotated pair densities

$$z_{lGi\bar{k}} = \sqrt{\frac{f_{i\bar{k}}}{V_s}} \sum_t \langle G | \Phi_l \Phi_t \rangle D_{ti}^{\bar{k},*}, \qquad (14)$$

and overlaps

$$\langle G | \Phi_l \Phi_t \rangle \equiv \int_{\text{elem. cell}} \Phi_l(R) \Phi_t(R) e^{-iGR} dR, \qquad (15)$$

and the exchange kernel is

$$v(G + k - \bar{k}) \equiv \int_{\text{supercell}} v(r) e^{-i(G+k-\bar{k})r} dr. \qquad (16)$$

$V_s$ denotes the supercell volume.

For $G \to 0$, $v$ in Eq.(16) could be singular, so we use a variant of the well-known Brillouin-supercell averaging.[27, 28] For details, see the SI.

Next, we split the summation over reciprocal lattice vectors to two parts, low and high: $Y_{pq}^k = Y_{pq}^{L,k} + Y_{pq}^{H,k}$. The numerical parameter separating low from high momenta, labeled $G_0$, is later varied to ensure convergence. For low-$G$, the summation is evaluated by explicitly applying Eq.(13) with $|G| < G_0$. For high $|G|$, we approximate

$$v(G - k + \bar{k}) \simeq v(G) \quad |G| > G_0. \qquad (17)$$

Then $Y_{jl}^{H,k} \simeq Y_{jl}^H$, i.e., independent of $k$. The $k$-point independent treatment of the high-$G$ space reduces the run-time for preparing the $z_{lGi\bar{k}}$ vectors (Eq.14) before the SCF cycle, taking less time than a $\Gamma$-point calculation.

The next step is the fragmented-stochastic-exchange formulation of Ref.[24],

$$\sum_G |G\rangle v(G) \langle G| = \frac{1}{N_\xi} \sum_\xi |\xi\rangle g_\xi \langle \xi|, \qquad (18)$$

where $\xi$ is a fragmented-stochastic basis, here made of a set of $N_\xi$ short random vectors in $G$ space, and $g_\xi$ is a sign vector indicating the sign of the exchange kernel $v(G)$. For periodic systems, $v(G)$ is purely positive, so $g_\xi = 1$. The equality above is formally true only in the limit $N_\xi \to \infty$, but in practice, the results converge rapidly so $N_\xi \sim 500$ is generally sufficient. Eq.(18) yields:

$$Y_{jl}^H \simeq -\sum_{i\bar{k}\xi} u_{j\xi i\bar{k}}^* g_\xi u_{l\xi i\bar{k}} \qquad (19)$$

with

$$u_{l\xi i\bar{k}} = \sqrt{f_{i\bar{k}}} \sum_t \langle \xi | \phi_l \phi_t \rangle D_{ti}^{\bar{k},*}. \qquad (20)$$

Note that $Y^L$ scales quadratically with the number of $k$-points, while $Y^H$ scales only linearly. It is therefore beneficial numerically to use a lower $G_0$, so that only a few $G$-vectors contribute to $Y^L$. We show later that the value of $G_0$ can be quite small, so that most $G$-vectors can be represented stochastically with the $N_\xi$ auxiliary basis, which does not grow with unit- or super-cell size.

Eqs.(12)-(20) give the complete expressions for the $X$ matrix. A technical point is that due to linear dependence considerations, the $B$ matrix is not square; only $\Phi_{jk}$ orbitals in the small exchange-active space $A$ are expanded, while their basis set, i.e., $\Phi_{j'}$ orbitals (Eq.10), encompasses the full active space $M$. For orbitals outside the exchange-active region, we could use a scissors-like expression,

$$X_{jl}^k = \delta_{jl} X_{\bar{j}\bar{j}}^k, \qquad (21)$$

for $j$ and $l$ in the lower $N_v - A_v$ space, where $\bar{j}$ is the lowest orbital in the exchange-active region $A$, and analogously for orbitals in the $N_c - A_c$ space. An alternative would be to include the contribution of orbitals outside the $A$ subspace stochastically.[29]

The hybrid-exchange approach presented here is benchmarked on various orthorhombic lattices, including traditional covalently-bonded diamond and silicon (Si), and molecular crystals with $\pi$-$\pi$ interactions: urea and 1,4-Bis-(2-methyl-phenyl)-benzene ($C_{20}H_{18}$).[30–32] The $C_{20}H_{18}$ unit cell consists of $\pi$-stacked layers of benzene rings arranged in a staggered geometry, see Fig.1.

LDA-DFT calculations on uniform $k$-grids are performed using Troullier-Martins NCPPs and a kinetic-energy cutoff of 25 a.u.[33, 34] These LDA simulations provide $k$-dependent energies (converged to $10^{-8}$ a.u.) and one-electron wavefunctions $\Phi_{jk}$ that serve as the initial basis. To ensure basis-set convergence the LDA-DFT calculations use at least five times more conduction than valence bands.

| Functional | $\alpha$ | $\beta$ | $\gamma$ |
|---|---|---|---|
| BNL | 0 | 1 | 0.11 |
| CL (CAM-LDA0) | 0.19 | 0.46 | 0.33 |
| HSE06 | 0.25 | -0.25 | 0.11 |
| PBE0 | 0.25 | 0 | 0 |

TABLE I. Hybrid exchange parameters per Eq.(3).

Electronic bandgaps, i.e., the difference between the conduction-band minimum (CBM) and valence-band maximum (VBM), are calculated with several hybrid functionals: BNL [13], CAM-LDA0 (CL) [35], HSE06, and PBE0. Table I shows the standard tabulated range-separation parameters used for CAM-LDA0 and HSE06. We use here the HSE06 value of $\gamma = 0.11$ Bohr$^{-1}$ for the BNL long-range hybrid.
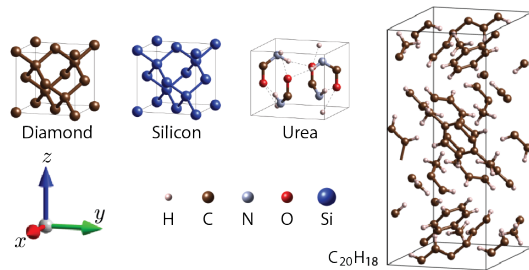


FIG. 1. Unit cells for systems studied.

| $k$-point Sampling | BNL | CL | HSE06 | PBE0 |
|---|---|---|---|---|
| $1 \times 1 \times 1$ | 3.73 | 4.87 | 1.77 | 2.50 |
| $2 \times 2 \times 2$ | 3.64 | 4.69 | 1.78 | 2.46 |
| $3 \times 3 \times 3$ | 3.88 | 4.58 | 1.84 | 2.57 |
| $4 \times 4 \times 4$ | 3.51 | 4.00 | 1.69 | 2.29 |
| $5 \times 5 \times 5$ | 3.79 | 4.18 | 1.74 | 2.48 |
| $6 \times 6 \times 6$ | 3.58 | 3.89 | 1.70 | 2.40 |
| $8 \times 8 \times 8$ | 3.61 | 3.78 | 1.73 | 2.44 |
| $10 \times 10 \times 10$ | 3.56 | 3.72 | 1.72 | 2.45 |

TABLE II. ngH-DFT bandgaps (eV) for Si lattices as a function of the $k$-point grid size for several functionals.

| $k$-point Sampling | BNL | CL | HSE06 | PBE0 |
|---|---|---|---|---|
| $1 \times 1 \times 1$ | 6.68 | 7.65 | 4.75 | 5.49 |
| $2 \times 2 \times 2$ | 6.31 | 6.90 | 4.37 | 5.04 |
| $3 \times 3 \times 3$ | 6.13 | 6.52 | 4.18 | 4.81 |
| $4 \times 4 \times 4$ | 5.91 | 6.38 | 4.15 | 4.75 |
| $5 \times 5 \times 5$ | 5.86 | 6.45 | 4.30 | 4.86 |
| $6 \times 6 \times 6$ | 5.74 | 6.32 | 4.22 | 4.78 |

TABLE III. ngH-DFT bandgaps (eV) for $C_{20}H_{18}$ (152-atom unit cell) for various functionals as a function of supercell size.

We first show results for small cell-size systems, specifically Si (additional data for diamond and urea is given in the SI). For small systems, the exchange-active space $A$ includes all valence orbitals and a large number of conduction orbitals. The cutoff parameter $G_0$ is converged so that for all functionals, the bandgaps agree within 10 meV with a fully deterministic calculation; $G_0 = 3$ a.u. is found sufficient for Si and diamond, and $G_0 = 2$ a.u. for urea. These are small values, so the number of $G$-vectors that need to be treated exactly per Eq.13 is only 6.1%, 1.8%, and 1.7% of the respective $G$-spaces.

Table II shows bandgaps for Si, where as well known, for global and long-range functionals, a large supercell is needed for convergence. Fig.2(a) shows the bandstructure of Si on a $10 \times 10 \times 10$ supercell with the long-range BNL XC functional. Bandstructures for other systems as well as comparisons to traditional non-stochastic methods [36] are provided in the SI.

We next move to a larger system, $C_{20}H_{18}$, with 152 atoms within a single unit cell. Fig.1 shows the unit cell, and Fig.2(b) provides the bandstructure on a supercell of 32,832 atoms using the BNL long-range hybrid. Table III provides bandgaps for various functionals as a function of supercell size. Due to the system's size, the molecular-orbital and exchange-active spaces are reduced to only include bands nearest to the Fermi level: $N_v = 100$, $N_c = 200$, $A_v = 50$, and $A_c = 100$. Selecting $N_v, A_v < N_{occ}$ (where $N_{occ}$ is the number of occupied valence bands) gives an error in the bandgap of roughly 200 meV, this could be remedied by a stochastic inclusion of the lower valence states, as in Ref. [29]. The results are mostly insensitive to $A_c$, the number of exchange-active conduction bands, as long as a sufficiently large $N_c$ is used. Further, $G_0 = 1$ a.u. here, so only 0.2% of the $G$-vectors are treated deterministically in the low-$G$ space while the remaining high-$G$ vectors are stochastically sampled with $N_\xi = 5000$ sparse-stochastic vectors.
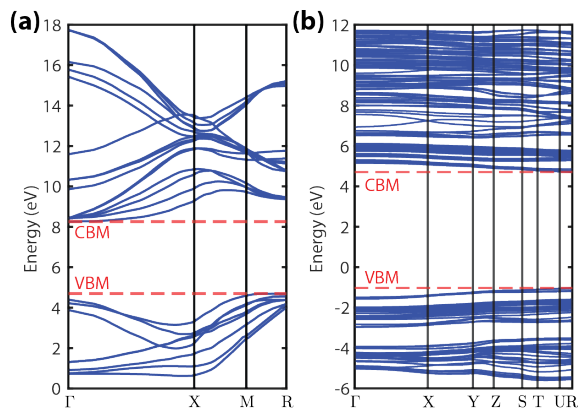


FIG. 2. Band structures of **(a)** Si on a $10 \times 10 \times 10$ $k$-grid and **(b)** $C_{20}H_{18}$ on a $6 \times 6 \times 6$ $k$-grid via the BNL functional. Special symmetry points are based on an orthorhombic lattice.
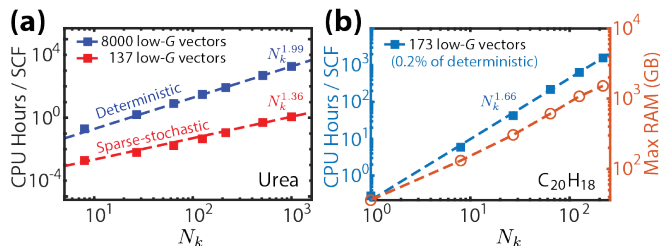


FIG. 3. CPU hours per SCF vs. number of $k$-points ($N_k$) on a logarithmic scale for **(a)** urea and **(b)** $C_{20}H_{18}$. For $C_{20}H_{18}$, maximum RAM usage is also shown as a function of $N_k$.

We now move to discuss the computational cost of the new approach. Fig.3 (a) shows the CPU scaling with the number of $k$-points for urea using the PBE0 hybrid. The scaling with $N_k$ remains quadratic for the fully

deterministic calculation (blue line), while the mixed deterministic/sparse-stochastic (red line) approach scales sub-quadratically with a much smaller prefactor. For example, the stochastic approach requires just 1 CPU hour per SCF iteration for a $10 \times 10 \times 10$ supercell, whereas a deterministic calculation demands approximately 2000 CPU hours per SCF.

Fig.3(b) shows the effective scaling of the method for $C_{20}H_{18}$. In addition to CPU scaling, the maximum RAM required is provided. The linear scaling of RAM requirements with supercell size is substantially lower than a conventional PW implementation of general hybrid-exchange.

Fig.4 shows the exponential convergence of the bandgap with the body-diagonal length $d$ of the supercells for urea and $C_{20}H_{18}$, respectively. This allows us to extrapolate to the thermodynamic limit, i.e., $d \to \infty$, with modest computational resources.

The stochastic error associated with sampling the high-$G$ exchange (i.e., $Y^H$) was studied for urea using the CAM-LDA0 and PBE0 hybrid functionals. With $N_\xi = 5000$, the sample standard deviation of the $\Gamma$-point bandgap is small, below 10 meV. The error becomes less than 2 meV for bandgaps calculated on larger supercells. The size of the sparse-stochastic basis could be reduced to even $N_\xi = 500$, as the (tiny) stochastic error stems primarily from the Monte-Carlo sampling of the $G \simeq 0$ parts of the exchange kernel.
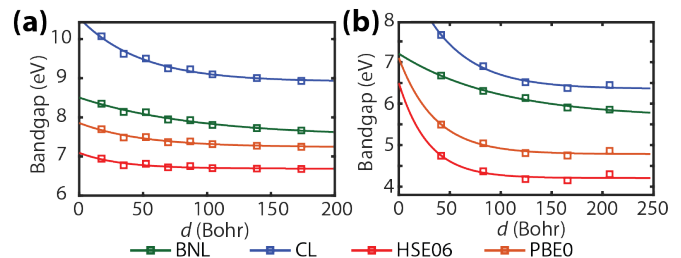


FIG. 4. Single-exponential fits of bandgaps against the body-diagonal length $d$ of the supercell for **(a)** urea and **(b)** $C_{20}H_{18}$.

In conclusion, we developed and benchmarked a grid-based PW implementation of GKS-DFT for periodic systems. The method scales gently with $k$-points and provides significant speedups to deterministic calculations. This approach enables extensive $k$-point sampling for DFT with any hybrid-exchange functional, including long-range hybrids. The GKS-DFT energies converge with less than ten SCF iterations. This makes the present method appealing for band-structure calculations and post-DFT excited-state approaches that require GKS energies and wavefunctions as inputs.

Future work will extend the static periodic ngH-DFT formalism to linear-response TDDFT for optical absorption spectra of solids. In the solid state, inclusion of a long-range Coulomb tail in the exchange kernel is re-

quired to produce excitonic effects and spectra in good agreement with experiment. [37, 38] In addition, this approach would be used to solve the GW-Bethe-Salpeter equation in extended systems where extensive $k$-point sampling is essential for accurate prediction of exciton binding energies. [39]

––––––––––

* dxn@ucla.edu

[1] Axel D. Becke, "Density-functional thermochemistry. III. The role of exact exchange," The Journal of Chemical Physics **98**, 5648–5652 (1993).

[2] Axel D. Becke, "A new mixing of Hartree-Fock and local density-functional theories," The Journal of Chemical Physics **98**, 1372–1377 (1993).

[3] A. Seidl, A. Görling, P. Vogl, J. A. Majewski, and M. Levy, "Generalized Kohn-Sham schemes and the band-gap problem," Phys. Rev. B **53**, 3764–3774 (1996).

[4] Thierry Leininger, Hermann Stoll, Hans-Joachim Werner, and Andreas Savin, "Combining long-range configuration interaction with short-range density functionals," Chemical Physics Letters **275**, 151–160 (1997).

[5] Benjamin G. Janesko, Thomas M. Henderson, and Gustavo E. Scuseria, "Screened hybrid density functionals for solid-state chemistry and physics," Phys. Chem. Chem. Phys. **11**, 443–454 (2009).

[6] Sivan Refaely-Abramson, Sahar Sharifzadeh, Manish Jain, Roi Baer, Jeffrey B. Neaton, and Leeor Kronik, "Gap renormalization of molecular crystals from density-functional theory," Phys. Rev. B **88**, 081204 (2013).

[7] Tamar Stein, Leeor Kronik, and Roi Baer, "Reliable prediction of charge transfer excitations in molecular complexes using time-dependent density functional theory," Journal of the American Chemical Society **131**, 2818–2820 (2009).

[8] Roi Baer, Ester Livshits, and Ulrike Salzner, "Tuned range-separated hybrids in density functional theory," Annual Review of Physical Chemistry **61**, 85–109 (2010).

[9] Jochen Heyd, Gustavo E. Scuseria, and Matthias Ernzerhof, "Hybrid functionals based on a screened Coulomb potential," The Journal of Chemical Physics **118**, 8207–8215 (2003).

[10] Jochen Heyd, Juan E. Peralta, Gustavo E. Scuseria, and Richard L. Martin, "Energy band gaps and lattice parameters evaluated with the Heyd-Scuseria-Ernzerhof screened hybrid functional," The Journal of Chemical Physics **123**, 174101 (2005).

[11] John P. Perdew, Kieron Burke, and Matthias Ernzerhof, "Generalized Gradient Approximation Made Simple," Physical Review Letters **77**, 3865–3868 (1996).

[12] Carlo Adamo and Vincenzo Barone, "Toward reliable density functional methods without adjustable parameters: The PBE0 model," The Journal of Chemical Physics **110**, 6158–6170 (1999).

[13] Roi Baer and Daniel Neuhauser, "Density functional theory with correct long-range asymptotic behavior," Phys. Rev. Lett. **94**, 043002 (2005).

[14] Jonathan H. Skone, Marco Govoni, and Giulia Galli, "Self-consistent hybrid functional for condensed systems," Physical Review B **89**, 195112 (2014).

[15] Jonathan H. Skone, Marco Govoni, and Giulia Galli, "Nonempirical range-separated hybrid functionals for solids and molecules," Physical Review B **93**, 235106 (2016).

[16] Chandrima Chakravarty, Maximilian A. C. Saller, Hüseyin Aksu, and Barry D. Dunietz, "Anisotropic dielectric screened range-separated hybrid density functional theory calculations of charge transfer states across an Anthracene–TCNQ donor–acceptor interface," Journal of Chemical Theory and Computation **20**, 10751–10758 (2024).

[17] Lin Lin, "Adaptively Compressed Exchange Operator," Journal of Chemical Theory and Computation **12**, 2242–2249 (2016).

[18] Xiao Wang, Cannada A. Lewis, and Edward F. Valeev, "Efficient evaluation of exact exchange for periodic systems via concentric atomic density fitting," The Journal of Chemical Physics **153**, 124116 (2020).

[19] Kai Wu, Xinming Qin, Wei Hu, and Jinlong Yang, "Low-rank approximations accelerated plane-wave hybrid functional calculations with k-point sampling," Journal of Chemical Theory and Computation **18**, 206–218 (2022).

[20] Sandeep Sharma, Alec F. White, and Gregory Beylkin, "Fast Exchange with Gaussian Basis Set Using Robust Pseudospectral Method," Journal of Chemical Theory and Computation **18**, 7306–7320 (2022).

[21] Sebastian Kokott, Florian Merz, Yi Yao, Christian Carbogno, Mariana Rossi, Ville Havu, Markus Rampp, Matthias Scheffler, and Volker Blum, "Efficient all-electron hybrid density functionals for atomistic simulations beyond 10000 atoms," The Journal of Chemical Physics **161**, 024112 (2024).

[22] Adam Rettig, Joonho Lee, and Martin Head-Gordon, "Even faster exact exchange for solids via tensor hypercontraction," Journal of Chemical Theory and Computation **19**, 5773–5784 (2023).

[23] Augustin Bussy and Jürg Hutter, "Efficient periodic resolution-of-the-identity Hartree–Fock exchange method with k-point sampling and Gaussian basis sets," The Journal of Chemical Physics **160**, 064116 (2024).

[24] Nadine C. Bradbury, Tucker Allen, Minh Nguyen, and Daniel Neuhauser, "Deterministic/Fragmented-Stochastic Exchange for Large-Scale Hybrid DFT Calculations," Journal of Chemical Theory and Computation **19**, 9239–9247 (2023).

[25] Mykola Sereda, Tucker Allen, Nadine C. Bradbury, Khaled Z. Ibrahim, and Daniel Neuhauser, "Sparse-Stochastic Fragmented Exchange for Large-Scale Hybrid Time-Dependent Density Functional Theory Calculations," Journal of Chemical Theory and Computation **20**, 4196–4204 (2024).

[26] Michael Rohlfing and Steven G. Louie, "Electron-hole excitations and optical spectra from first principles," Phys. Rev. B **62**, 4927–4944 (2000).

[27] Sohrab Ismail-Beigi, "Truncation of periodic image interactions for confined systems," Physical Review B **73**, 233103 (2006).

[28] Ravishankar Sundararaman and T. A. Arias, "Regularization of the Coulomb singularity in exact exchange by Wigner-Seitz truncated interactions: Towards chemical accuracy in nontrivial systems," Phys. Rev. B **87**, 165122 (2013).

[29] Nadine C. Bradbury, Tucker Allen, Minh Nguyen, Khaled Z. Ibrahim, and Daniel Neuhauser, "Optimized attenuated interaction: Enabling stochastic Bethe–Salpeter spectra for large systems," The Journal of Chemical Physics **158**, 154104 (2023).

[30] T. Hom, W. Kiszenik, and B. Post, "Accurate lattice constants from multiple reflection measurements. II. Lattice constants of germanium silicon, and diamond," Journal of Applied Crystallography **8**, 457–458 (1975).

[31] H. Guth, G. Heger, S. Klein, W. Treutmann, and C. Scheringer, "Strukturverfeinerung von harnstoff mit neutronenbeugungsdaten bei 60, 123 und 293 k und x-n- und x-x(1s2)-synthesen bei etwa 100 k," Zeitschrift für Kristallographie - Crystalline Materials **153**, 237–254 (1980).

[32] Lodovico Lunazzi, Andrea Mazzanti, Mirko Minzoni, and J. Edgar Anderson, "Structure, conformation, and dynamic processes of the stereolabile atropisomers of hindered terphenyl hydrocarbons," Organic Letters **7**, 1291–1294 (2005).

[33] John P. Perdew and Yue Wang, "Accurate and simple analytic representation of the electron-gas correlation energy," Phys. Rev. B **45**, 13244–13249 (1992).

[34] N. Troullier and José Luís Martins, "Efficient pseudopotentials for plane-wave calculations," Phys. Rev. B **43**, 1993–2006 (1991).

[35] Takeshi Yanai, David P Tew, and Nicholas C Handy, "A new hybrid exchange–correlation functional using the Coulomb-attenuating method (CAM-B3LYP)," Chemical Physics Letters **393**, 51–57 (2004).

[36] Paolo Giannozzi, Oscar Baseggio, Pietro Bonfà, Davide Brunato, Roberto Car, Ivan Carnimeo, Carlo Cavazzoni, Stefano de Gironcoli, Pietro Delugas, Fabrizio Ferrari Ruffino, Andrea Ferretti, Nicola Marzari, Iurii Timrov, Andrea Urru, and Stefano Baroni, "Quantum Espresso toward the exascale," The Journal of Chemical Physics **152**, 154105 (2020).

[37] Lucia Reining, Valerio Olevano, Angel Rubio, and Giovanni Onida, "Excitonic effects in solids described by time-dependent density-functional theory," Phys. Rev. Lett. **88**, 066404 (2002).

[38] Guy Ohad, Stephen E. Gant, Dahvyd Wing, Jonah B. Haber, María Camarasa-Gómez, Francisca Sagredo, Marina R. Filip, Jeffrey B. Neaton, and Leeor Kronik, "Optical absorption spectra of metal oxides from time-dependent density functional theory and many-body perturbation theory based on optimally-tuned hybrid functionals," Phys. Rev. Mater. **7**, 123803 (2023).

[39] Antonios M. Alvertis, Aurélie Champagne, Mauro Del Ben, Felipe H. da Jornada, Diana Y. Qiu, Marina R. Filip, and Jeffrey B. Neaton, "Importance of nonuniform Brillouin zone sampling for ab initio Bethe-Salpeter equation calculations of exciton binding energies in crystalline solids," Phys. Rev. B **108**, 235117 (2023).